Linker Conformation Controls Oxidation Potentials and Electrochromism in Highly Stable Zr-Based Metal−Organic Frameworks

Leonid Shupletsov,[#] Sebahat Topal,[#] Alina Schieck, Stella Helten, Ronny Grünker, Antareekshya Deka, Ankita De, Matthias Werheid, Volodymyr Bon, Inez Weidinger, Andreas Pöppl, Irena Senkovska,* and Stefan Kaskel*

ABSTRACT: The development of tailor-made electrochromic (EC) materials requires a large variety of available substances with properties that precisely match the task. Since the inception of electrochromic metal−organic frameworks (MOFs), the field relies only on a limited set of building blocks, providing the desired electrochromic effect. Herein, we demonstrate for the first time the implementation of a Piccard-type system (*N*,*N*,*N*′,*N*′-benzidinetetrabenzoate) into Zr-MOFs to obtain electrochromic materials. With fast switching rates, high contrast ratio, long-life stability, and exceptional chemical and physical stability, the novel material is on par with inorganic EC material. The new EC system exhibits an ultrahigh contrast from the bleaching state, with transmittance in the visible region >53%, to the colored state with a transmittance of ca. 3%. The 5 μm thick film attained up to 90% of the coloring in 12.5 s and exhibited high electrochemical reversibility. Moreover, the conformational lability of the electrochromic ligand chosen is locked via the topology design of the framework, which is not attainable in the solution. Locked conformations of the redox active linker in distinct polymorphous frameworks (DUT-65 and DUT-66) feature different redox characteristics and opens the door to the overarching control of the oxidation pathway in the Piccard-type systems.

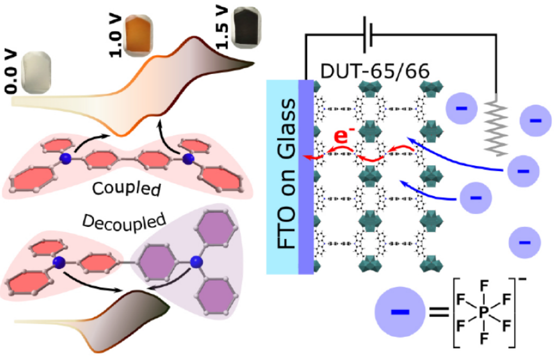

INTRODUCTION

The modular construction principles of metal−organic frameworks (MOFs) allow targeted control of their pore sizes and geometry, as well as their surface chemistry,[1−3] offering the possibility for tailor-made materials for a wide range of potential applications, increasingly involving their electrical properties, such as in supercapacitors, batteries, light-emitting diodes, electrocatalysts,[4,5] or sensors, and also electrochromic devices.[6,7]

MOFs have an ordered structure determined mostly by the coordination of the metal and the geometry of the linkers with a high degree of synthetic control that allows their intrinsic electrical properties to be tuned. Their porosity provides opportunities to introduce non-native functionality by insertion of the guest molecules into the pores.[8] Crystallinity and low concentration of defects, typical for MOF materials, may eliminate the vast disorder that is a major contributor to poor mobility and low carrier densities in organic conductors relative to those in crystalline inorganic materials such as silicon.

The electrical conductivities of MOFs can arise from different mechanisms. Besides the *through bond* or *through space*, a special class of MOFs also demonstrate a pure *redox-hopping* mechanism of conduction.[9−11] In this case, the hopping of electrons (or holes) between neighboring redox centers is coupled to the motion of counterbalancing ions. Hence, the porosity is the prerequisite for such type of conductivity since the diffusion of ions is the rate-determining step.[12,13]

One emerging property of a part of electrically conductive MOFs based on redox-active linkers is the electrochromic (EC) behavior. EC materials represent an innovative category of electronically reconfigurable substances capable of dynamically switching their optical properties. These materials have found diverse applications related to display technology, which necessitates a wide array of materials endowed with adjustable optical characteristics. MOFs have been relatively little

Scheme 1. Oxidation and Reduction Mechanism of R_4BenzTB

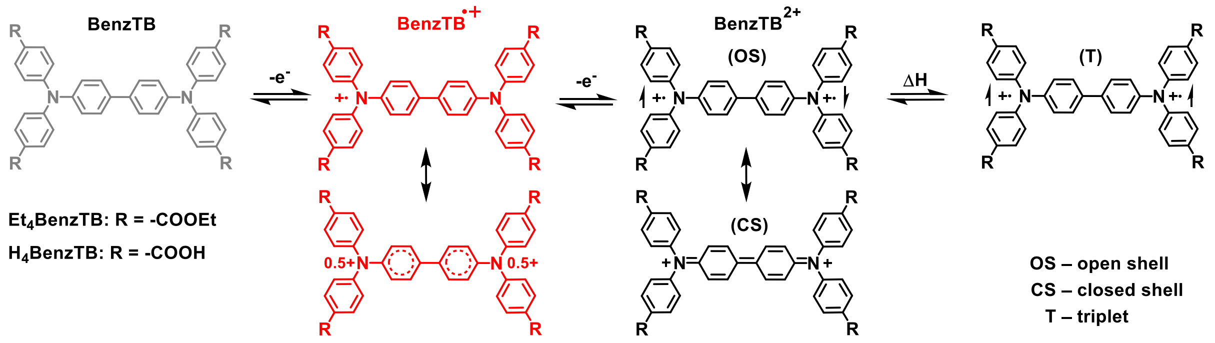

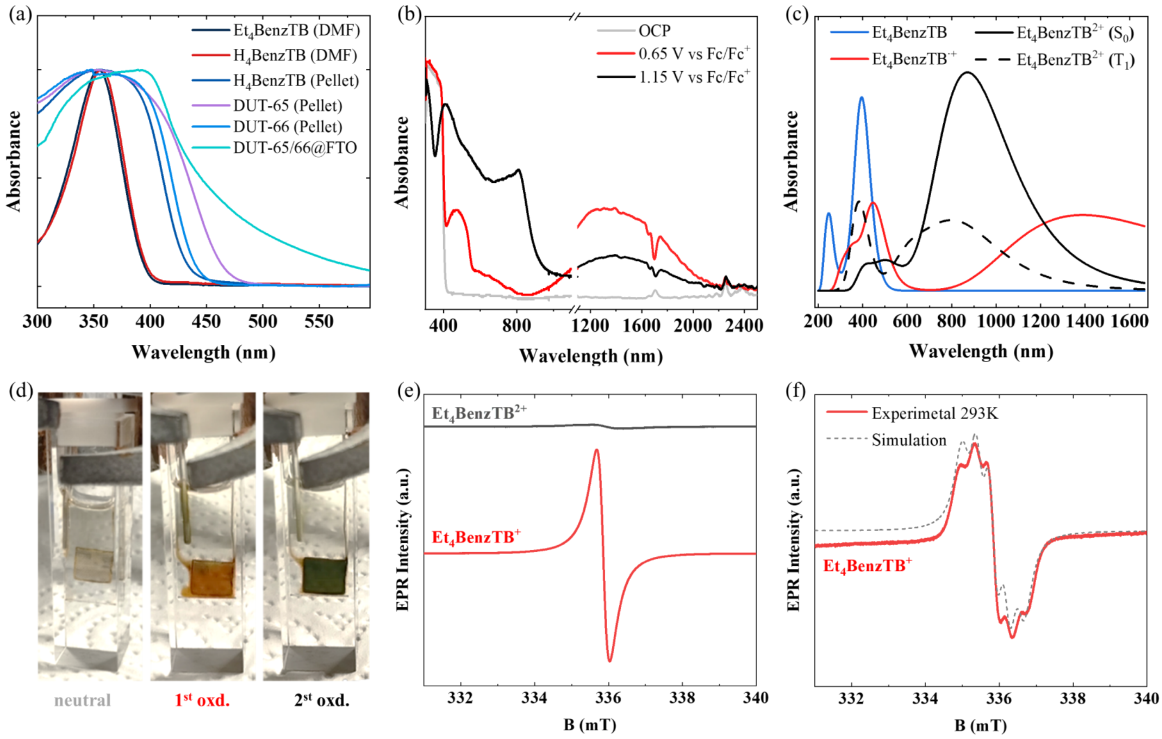

Figure 1. (a) UV−vis absorption spectra of H_4BenzTB and Et_4BenzTB solutions (1 mM) in DMF measured in transmission. Solid state measurements of H_4BenzTB, DUT-65, and DUT-66 measured as pellet with $BaSO_4$ in reflection and DUT-65/66@FTO measured in transmission. (b) UV−vis−NIR spectra of Et_4BenzTB (1 mM) at different potentials in 0.1 M TBA PF_6/DCM. (c) Absorption spectra of Et_4BenzTB, $Et_4BenzTB^{•+}$ and $Et_4BenzTB^{2+}$ simulated by TD-DFT. (d) Photos of Et_4BenzTB solution (1 mM) at different potentials in 0.1 M $TBAPF_6$/DCM, Pt-mesh as working and Pt-wire as counter electrodes. (e) EPR spectrum of chemically oxidized Et_4BenzTB at 160 K in DCM. (f) EPR spectrum of $Et_4BenzTB^+$ at RT in DCM and corresponding simulated spectrum.

explored as EC materials, although their modularity and porosity offer promising avenues for precise control over electrochromic behavior. In general, three different redox-active mechanisms are observed in EC MOFs, as the redox activity can occur at the metal sites,[14] the linker,[15] or adsorbed guest molecules.[16] Currently, the vast majority of published EC MOFs or EC covalent−organic frameworks (COFs)[17−21] rely on redox-active linkers,[11,22,23] in which the most frequently reported linkers for MOFs until now are based on a naphthalene diimide,[6,24−27] perylene diimide,[27] pyrene,[7,28] or tritopic triphenylamine derivatives.[29−31] But electronic properties of tetratopic bistriarylamine-based MOFs have received little attention until now, although bistriarylamine based molecules are known to have mixed-valence character, strong coupling of redox centers, and ultrafast electron transfer.[32]

Herein, we propose a tetratopic, bistriarylamine-derived linker—*N*,*N*,*N*′,*N*′-benzidinetetrabenzoate (BenzTB, Scheme 1)—forming stable diradical cations as an efficient building block for EC MOFs.

The electrochemical and electrochromic properties of such radical or diradical systems, originally discovered more than a century ago by Gomberg (1900),[33] Chichibabin (1907),[34] and Piccard (1913),[35−37] were extensively studied in the past,[38−42] and such molecules were readily employed in organic solar cells[43] and OLEDs.[44]

However, despite the reported intense colors of the Chichibabin hydrocarbon and the isoelectronic cation of the Piccard system, their implementation as EC materials has remained undervalued to this day.

The Piccard-type system forms a stable open-shell (OS) singlet diradical cation with strong light-absorbing properties

Table 1. Summary of Experimental and Calculated UV-Vis Absorption Maxima, Calculated Dihedral Angles of the Linker in Solution, and Relative Energies of the Closed Shell and Triplet States Compared with the Open Shell State[a]

	$Et_4BenzTB^{\pm 0}$	$Et_4BenzTB^{\bullet +}$	$Et_4BenzTB^{2+}$ (CS)	$Et_4BenzTB^{2+}$ (OS)	$Et_4BenzTB^{2+}$ (T)
λ_{max}/nm (calc)	248, 397	454, 1389		436, 501, 871	387, 800
λ_{max}/nm (exp)	357	475, 1350^{b}		410, 811, 1400^{b}	
Dihedral angle Θ/deg	38.0	24.5	17.0	20.1	27.2
$(E_X - E_{OS})$/kcal·mol^{-1}			0.21	0.0	4.11

[a]The superscript ^{b} indicates a broad peak.

upon oxidation. The oxidation consists of two distinct single electron transfers (SETs), allowing for additional color variability.[45] We targeted the incorporation of BenzTB into a MOF to achieve spatial separation and, thus, to further stabilize the radical species. This may provide a memory effect to the EC color change, which is highly desired in EC devices.[46]

Incorporation of Chichibabin's hydrocarbon motif into π-conjugated polyradicaloid molecular cages connected by two benzene-1,3,5-triyl bridgeheads was first demonstrated by Wu et al.[47] Recently, similar systems, such as Thiele[48] and Müller[49] hydrocarbon analogues, were reported in MOFs[50] and COFs.[51] BenzTB as a tetratopic linker was also utilized, i.e., by our group, for the construction of MOFs with high porosity and solvent-dependent fluorescence. In conjunction with Zn_4O^{6+} or paddle wheel clusters, SNU-25,[52] DUT-10,[53] DUT-13,[54,55] and DUT-25[56] have been synthesized. Also, In- and Cd-based MOFs have been reported.[57−60]

In the following, we report the synthesis and structure of two chemically stable Zr-based MOFs as well as their electrochromic properties. The conformational lability of the BenzTB enables control of the conformation and locking of the linker conformation via the topology of the framework,[61] which is unattainable in solution. We demonstrate this strategy through the deliberate design of two novel polymorphic frameworks $[Zr_6O_4(OH)_4(BenzTB)_2(L)_4]_n$ (DUT-65, DUT-66; DUT—Dresden University of Technology; L—modulator), which differ in their topology. The framework imposes a defined geometry for the BenzTB molecules with a specific dihedral twisting angle for tuning their redox behavior.[39] Analyzing the two dimorphic MOFs, DUT-65 and DUT-66, differing in linker conformation, elucidates the mere influence of the twisting angle on the redox process of the linker without any other chemical modifications. Thus, the incorporation of BenzTB into a MOF offers a unique opportunity to study the impact of conformational isomerism without the need for additional constitutional changes to the molecule.

Since the carboxylate groups of the BenzTB allow for a facile grafting of the MOF on transparent conductive oxides (TCO) (e.g., fluorine-doped tin oxide, FTO) via a preceding self-assembled monolayer formation,[62,63] MOF thin films demonstrating short switching times, high optical modulation and long-term stability could be prepared. We highlight the multitude of color responses provided by the $[Zr_6O_4(OH)_4(BenzTB)_2(L)_4]_n$ framework as a platform for versatile EC applications.

RESULTS AND DISCUSSION

Piccard-System Based Linkers. The desired $H_4BenzTB$ linker (Scheme 1) was obtained in a high-yield two-step synthesis from benzidine and ethyl 4-bromobenzoate with subsequent alkaline hydrolysis (Scheme S1).[53] Despite the long history of the Piccard system, the redox behavior of the tetracarboxylate derivative has been rather unexplored. The strong electron-withdrawing effect of the carboxylates is expected to impact the redox behavior of the system and shift the oxidation potential to higher potentials.

First, optical and electrochemical characterization of the ligand was performed and supported by density-functional theory (DFT) calculations and electron paramagnetic resonance (EPR) spectroscopy. The ethyl ester of the linker ($Et_4BenzTB$) was chosen as a model compound, which demonstrated the same optoelectronic properties as the free acid (Figure 1a) with the advantage of adequate solubility in various organic solvents. In the cyclic voltammogram (CV) two redox events occur at formally $E_{1/2}{}^{0/\bullet +}$ = 0.59 V and $E_{1/2}{}^{\bullet +/2+}$ = 0.72 V vs Fc/Fc$^+$, respectively, corresponding to the $Et_4BenzTB^{0/\bullet +}$ and $Et_4BenzTB^{\bullet +/2+}$ redox couples resulting in a small $\Delta E_{1/2}$ of only 0.13 V (Figure S3).

As expected, the electron-withdrawing effect of the carboxylate groups shifts the redox reactions to higher potentials compared to the nonfunctionalized compounds or compounds with electron-donating groups, such as methyl or methoxy.[32,39,45] Meanwhile, the potential difference between the first and second redox processes is smaller than in the above-mentioned cases (see Table S1). The small potential difference between the two redox steps indicates weak stabilization of the $Et_4BenzTB^{\bullet +}$ moiety. The charge is thus more localized at one of the nitrogen atoms, as was demonstrated by Kaafarani et al. in similar systems.[42]

The reversible oxidation of $Et_4BenzTB$ causes a color change, which can be monitored *via operando* ultraviolet−visible (UV−vis) spectroscopy. The stepwise oxidation of the moiety allows a deliberate switching between three states, thus three "main" colors: the nonoxidized, the cation radical, and the dicationic forms (Figure 1b−d). Room temperature UV−vis−near-infrared (NIR) spectroelectrochemical studies of $Et_4BenzTB$ oxidation in dichloromethane (DCM) were undertaken (Figure 1b) and supported by time-dependent density functional theory (TD-DFT) calculations.

For all three species, the calculated absorption spectra are in reasonable agreement with the experimental data (Figure 1b,c and Table 1). For the $Et_4BenzTB$, the absorption maximum at <400 nm arises from the highest occupied molecular orbital (HOMO) → lowest unoccupied molecular orbital (LUMO) transition with admixtures of the HOMO-1 and HOMO-2 → LUMO transitions. The cationic radical $Et_4BenzTB^{\bullet +}$ demonstrates two distinct maxima. The NIR range absorption with a maximum at 1350 nm and the main visible range absorption with a maximum at 475 nm can be attributed to the HOMO → singly occupied molecular orbital (SOMO) and the SOMO → LUMO transitions, respectively. The predicted spectrum has only a minor deviation from the experimental data in the vis range, showing a discrepancy in the absorption maximum of less than 20 nm, while the NIR range is in perfect agreement.

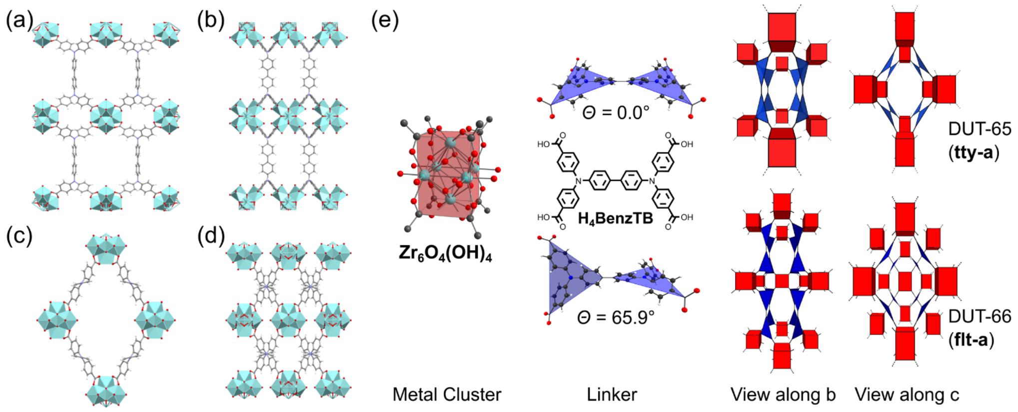

Figure 2. View along: (a) *a*-axis of DUT-65 and DUT-66, (b) along *b*-axis of DUT-65 and DUT-66; (c) along *c*-axis of DUT-65; and (d) along *c*-axis of DUT-66. The modulator molecules as well as H atoms are not shown. (e) Topological deconstruction of DUT-65 and DUT-66 and adopted dihedral angle Θ of the BenzTB linker in the eclipsed (top) and staggered (bottom) forms. The hydrogen atoms are omitted. Only the oxygen atoms of the modulator molecules in the Zr-cluster are shown.

In the case of the $Et_4BenzTB^{2+}$ diradical cation, two TD-DFT calculations are performed, for both the OS singlet (S_0) and the triplet (T_1) state (Scheme 1). Both states are initially considered, although the calculations suggest a 4.1 kcal mol^{-1} energy difference between them, indicating that the triplet state is almost nonpopulated at room temperature. The Boltzmann distribution provides a Boltzmann factor of 1.06×10^{-3}, implying that only approximately 0.1% of the $Et_4BenzTB^{2+}$ can access the triplet state at room temperature. In both cases, the calculations suggest strong absorption in the entire visible range, tailing out to the NIR range. This matches well with the experimental observations, although the peak shape and intensities demonstrate clear discrepancies with the experimental data.

The maximum absorption peak in the calculated spectrum appears at 870 nm for the singlet state and at 796 nm for the triplet, whereas the experimental spectrum shows a local maximum at 811 nm. This absorption can be attributed to the HOMO → LUMO excitation of the singlet and the HOMO → SOMO transition of the triplet. The experimental data, however, also demonstrate a strong absorption in the NIR range similar to the one observed for $Et_4BenzTB^{\bullet+}$.

This transition is not expected for $Et_4BenzTB^{2+}$, which indicates either an incomplete second oxidation of the compound during the measurement or a reaction of $Et_4BenzTB^{2+}$, resulting in its reduction. For instance, a comproportionating of $Et_4BenzTB^{2+}$ with remaining pristine $Et_4BenzTB$ in solution to $Et_4BenzTB^{\bullet+}$ is likely possible.

To confirm the radical character of the linker, the mono- and dicationic forms of $Et_4BenzTB$ were oxidized chemically with $Ag[SbF_6]$ and $NO[SbF_6]$ in DCM to obtain $Et_4BenzTB^{\bullet+}$ and $Et_4BenzTB^{2+}$, respectively. The oxidation potentials of Ag/Ag^+ and NO/NO^+ in DCM are 0.65 and 1.00 V vs. the Fc/Fc^+ redox couple, respectively.[64] Conveniently the oxidation potential of Ag^+ is right between the $E_{1/2}{}^{0/\bullet+}$ and $E_{1/2}{}^{\bullet+/2+}$ of $Et_4BenzTB$. Thus, defined oxidation states of $Et_4BenzTB$ could be achieved and characterized by UV−vis and EPR spectroscopy (Section S2.6 and Figure S5). The monocationic $Et_4BenzTB^{\bullet+}$ exhibits pronounced paramagnetic EPR behavior. Meanwhile, the dicationic $Et_4BenzTB^{2+}$ shows no EPR signals, except for one originating from residual monoradical impurities in the sample (Figure 1e). This confirms the predicted singlet state of the dication and the negligible number of the triplet population. The observed spectra are well in line with data previously published on similar compounds.[45,65−68]

Synthesis and Characterization of the Zr-Based MOFs (DUT-65 and DUT-66) Involving BenzTB Ligand and DUT-65/66 MOF Film. The $H_4BenzTB$ could be successfully utilized as a ligand for synthesizing porous Zr-based MOFs in the presence of benzoic, formic, or acetic acids as modulators. The synthesis resulted in the concomitant formation of single crystals of two polymorphic compounds with a similar composition $[Zr_6O_4(OH)_4(BenzTB)_2(L)_4]_n$ but differing in topology, further referred to as DUT-65 and DUT-66. The single crystal analysis shows (for more details, see Section S4) that both obtained polymorphs constitute 4,8-connected nets involving Zr_6-clusters with reduced connectivity and are isoreticular to PCN-605 and PCN-606.[61] The polymorphism arises from the conformation of the linker, adopting eclipsed or staggered forms (Figure 2e). The polymorph involving the eclipsed form of BenzTB (C_2 symmetry) gives rise to the **scu-a** topology (DUT-65). However, as a tetrahedral node in staggered conformation (D_2 symmetry), it forms a **flu-a** network (DUT-66, the linker is considered as a 4-connecting node, Figure S7). Considering the guidelines provided by O'Keeffe and Yaghi, where each branching point of the organic linker should be regarded as a separate node of the net,[69] the BenzTB can be deconstructed into two 3-C vertices. Thus, the underlying net of DUT-65 becomes **tty-a** and that of the DUT-66 **flt-a** topology (Figure 2e).

Both frameworks crystallize in an orthorhombic crystal system: DUT-65 in *Cmmm* and DUT-66 in *Fmmm* space group (Table S6). When the structures along the crystallographic axes are examined, the views along *a*- and *b*-axes appear identical for both compounds. A prominent difference is visible in the view along the respective *c*-directions: In DUT-65, diamond-shaped channels are formed by the interconnection between the Zr-clusters and the BenzTB linkers. In DUT-66, the staggered conformation of the BenzTB linkers blocks the channel in this direction by generating an AB-type arrangement of SBUs (Figure 2a−d).

Both DUT-65 and DUT-66 phases are likely to be obtained as a mixture (Figure 3) and can even cocrystallize in the same single crystal, as confirmed by the single crystal X-ray diffraction. The refinement of the occupancy of the atom

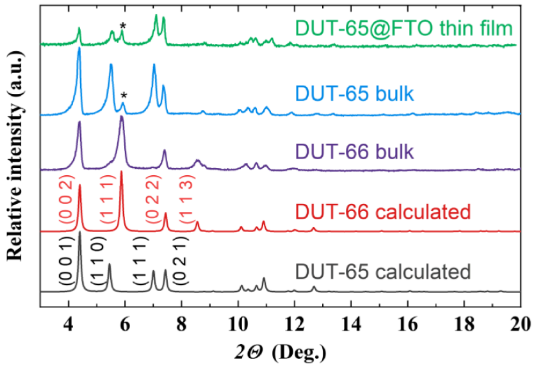

Figure 3. Experimental PXRD patterns of bulk DUT-65 (blue) and DUT-66 (purple) materials. PXRD pattern of thin film grown on FTO substrate (green). The patterns calculated from the crystal structures of DUT-65 and DUT-66 are shown in black and red, respectively.

positions shows the ratio of the DUT-66 to DUT-65 (and *vice versa*) domains to be approximately 4:1 (Section S4). Thus, each polymorph always contains a small fraction of the other phase.

Typically, the fraction of the DUT-66 phase increases for the powdered samples obtained at lower temperatures, lower modulator amounts, and, consequently, shorter synthesis time (for more details, see Section S3). It is challenging to obtain DUT-66 as large single crystals, and it requires lower temperatures than the DUT-65 (80 °C vs. 120 °C) (Figure S6a). Both observations suggest that the DUT-66 phase has a lower formation barrier but is less thermodynamically stable than the DUT-65 phase. Furthermore, the water content of the synthesis mixture is crucial for the formation of the DUT-66 phase. For instance, by substituting $ZrCl_4$ with $ZrOCl_2{\cdot}xH_2O$ ($6 < x < 8$) or by substituting the benzoic acid modulator with formic acid, a microcrystalline DUT-66 could readily be synthesized (Figure S6c). The formation of DUT-66 phase is also promoted by choosing *N,N*-dimethylformamide (DMF) as a solvent instead of *N,N*-diethylformamide (DEF), since the decomposition of the formic acid and DMF at elevated temperatures in the acidic medium of the synthesis mixture may result in water formation.[70] This apparently changes the kinetics of crystallization and promotes faster formation of the **flt-a** topology.

The torsion strain of the linker, determined by DFT calculation, reveals the reasons for the formation of the two observed topologies (Section S2.4). The calculation shows that the increase in the total energy induced by the geometrical strain is equally large for both conformations in the nonoxidized BenzTB. From the relaxed geometry with dihedral angle (Θ) of 37°, the total energy of the molecule increases by 0.50 kcal/mol to allow for the **tty-a** topology with dihedral angle of 0.0° and by 0.50 kcal/mol to allow for the **flt-a** topology with Θ = 65.9°. This value is below the accuracy of the DFT method,[71] which implies that the two configurations are quasi-isoenergetic.

Geometric analysis of the porosity of the two structures applying Mercury software[72] results in one-dimensional channels for both compounds with the maximum pore diameter of 13.2 and 12.2 Å for DUT-65 and DUT-66, respectively (Table S7, ESI). The limiting pore diameters are 9.7 Å in the case of DUT-65 and 10.2 Å in the case of DUT-66. The calculated helium-accessible pore volume is 1.20 cm^3 g^{-1} for DUT-65 and 1.11 cm^3 g^{-1} for DUT-66. The expected

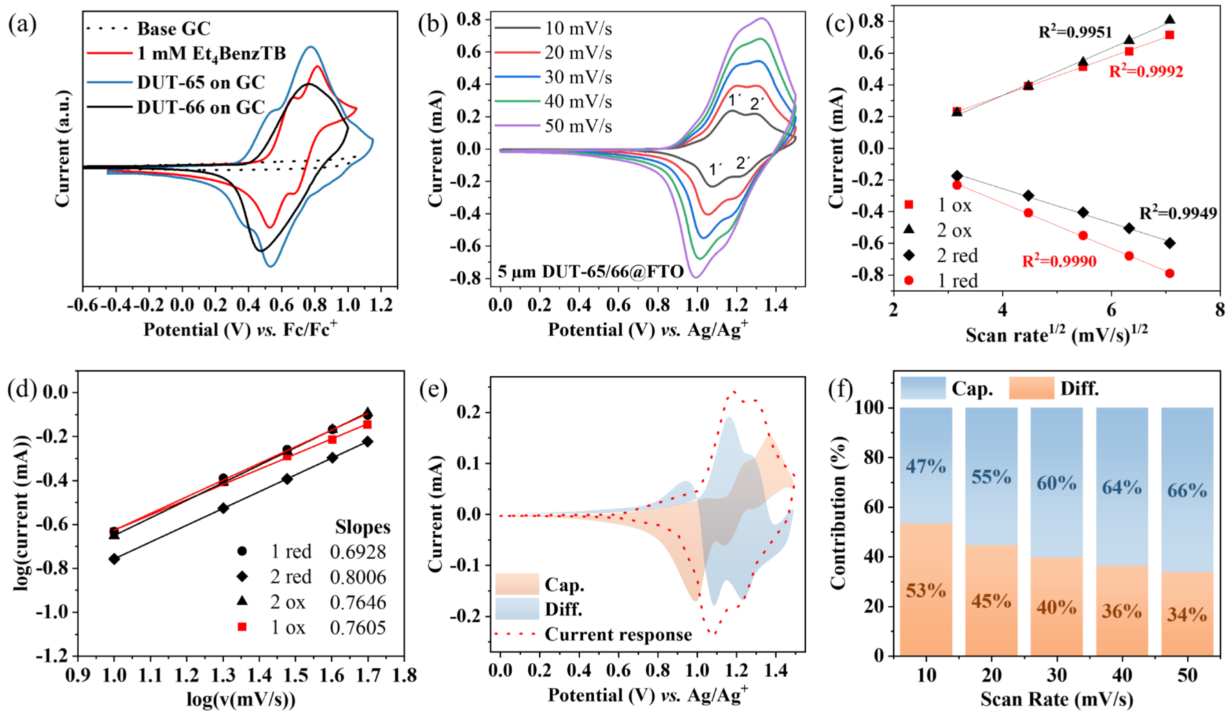

Figure 4. (a) CV of $Et_4BenzTB$ (1 mM) in 0.1 M $TBAPF_6$/DCM, DUT-65, and DUT-66 composites on GC in 0.1 M $TBAPF_6$/ACN. (b) Scan rate dependent CV measured on the MOF film on FTO substrate. (c) The peak current density vs (scan rate)$^{1/2}$. (d) Logarithmic current–potential plot. (e) Dunn's method analysis of diffusion contribution at 10 mV s^{-1}; (f) Histogram showing the contribution of capacitance and diffusion at different scan rate of DUT-65/66@FTO in 0.1 M $TBAPF_6$/ACN.

specific surface areas are 2810 m^2 g^{-1} and 2721 m^2 g^{-1}, respectively.

The experimental open pore porosity could not be derived from the nitrogen physisorption isotherms due to the flexibility of the frameworks and the structural pore closing transition upon solvent removal (Figure S10c,d).[61] Since the accessibility of the pores in the liquid phase is more important for the envisioned application as an EC material, it was verified by dye adsorption experiments. For this purpose, the crystals were soaked in ethanol solutions of the following dyes: Nile red, brilliant green, methylene blue, Reichardt's Dye, and rhodamine B. All the molecules, except Reichardt's dye, could enter the pores of DUT-65 and DUT-66 and be adsorbed, as can be seen from the color change of the crystals (Table S8).

Hence, DUT-65 and DUT-66 are ideal candidates for EC studies, providing the EC linker and pores that are accessible for the ions. Moreover, MOFs demonstrated remarkable chemical stability. The samples soaked in water for 3 days retained crystallinity, according to powder X-ray diffraction (PXRD) data (Figure S6d), and no detectable linker leaching according to liquid UV−vis analysis of the supernatant was observed.

A different approach had to be chosen to synthesize the MOF films on FTO since the methods described above led to the formation of large crystals rather than homogeneous polycrystalline powders. For the film synthesis, acetic acid was employed as a modulator, and the linker-to-metal ratio was adopted (Table S5). Scanning electron microscopy (SEM) analysis of the MOF@FTO confirmed the homogeneity of the obtained films. The thickness of the films is readily controlled by the synthesis time, allowing for the formation of 1 to 30 μm thick films (see SI section 6). Considering the obtained XRD pattern of the MOF thin films, the intensities of the peaks at $2\Theta = 5.45°$ (indicative of DUT-65) and at $2\Theta = 5.87°$ (indicative of DUT-66) are almost identical, which suggests the coexistence of the two phases in the film. Moreover, both conformers can coexist in one single crystal (see SI section 4). The intensity of (001) peak at $2\Theta = 4.41°$ is reduced compared to the bulk sample (Figure 3), pointing to the oriented growth of the crystals on the substrate.

Electrochemical Behavior of DUT-65, DUT-66, and DUT-65/66 MOF@FTO Film. To study the redox properties of the compounds with a predominant conformation, CVs of DUT-65 and DUT-66 were measured on MOF-containing composites prepared from a slurry with graphitized carbon and poly(vinylidene fluoride) (PVDF) additives on a glassy carbon (GC) electrode.

DUT-65, involving eclipsed linker conformation, shows reversible redox waves with two anodic ($E_a^1 = 0.56$ and $E_a^2 = 0.77$ V vs Fc/Fc$^+$) and two cathodic ($E_c^1 = 0.38$ and $E_c^2 = 0.53$ V vs Fc/Fc$^+$) peaks that are assigned to BenzTB$^{0/\bullet+}$ and BenzTB$^{\bullet+/2+}$ couples with redox potentials at formally $E_{1/2}{}^{0/\bullet+} = 0.47$ and $E_{1/2}{}^{\bullet+/2+} = 0.65$ V vs Fc/Fc$^+$, respectively (Figure 4a). In both cases, the two peaks correspond to two distinct one-electron oxidation waves at each nitrogen redox center.[73] The redox potentials of the BenzTB are slightly shifted to lower potentials for the DUT-65 MOF compared to those of the free Et_4BenzTB molecule. The shifts amount to 0.12 V for BenzTB$^{0/\bullet+}$ and 0.07 V for BenzTB$^{\bullet+/2+}$ redox couples and likely arise from the strain on the linker induced by the MOF topology.

DUT-66, involving staggered linker conformation, however, demonstrates only one redox wave with an anodic peak at $E_a = 0.76$ V vs Fc/Fc$^+$ and a cathodic peak at $E_c = 0.47$ V vs Fc/Fc$^+$ (Figure 4a). Obviously, the two distinct SETs, observable for the free linker and DUT-65, merge. This observation is also supported by differential pulse voltammetry (DPV) (Figure S11).

It is evident that the twisting of the molecule influences its redox behavior and narrows the potential gap between the first and second oxidation. The constraint imposed on the linker by the MOF does not allow for the sufficient stabilization of the oxidized state. A stabilization can only effectively occur in a more planar conformation of the linker (as in the case of DUT-65), which allows for a mesomeric stabilization of the oxidized state through the aromatic system, as depicted in Scheme 1. The findings are in line with previous theoretical calculations as well as crystallographic studies showing that oxidation of the BenzTB core would be accompanied by planarization and adoption of partial quinoidal character in the biphenyl group, with rotation of the peripheral aryl groups about the N−C aryl bond.[39,41]

The dihedral twist imposed by the MOF results in a strong electronic decoupling of the two amines in the molecule.[39] Calculations confirm the increase of the diradical character for the more twisted conformation as well as the lowering of the energy barrier between the singlet and triplet states. The difference in energy between HOMO and HOMO-1 (Table S4), conceptually connected to the delocalization of holes, points in the case of DUT-66 on the weaker coupling between triphenylamines in comparison to DUT-65. This also suggests a higher reactivity of the dicationic form of the linker in the staggered conformation.

The different behaviors of DUT-65 and DUT-66 during oxidation and reduction underline the possibility of controlling the redox behavior of the linker molecules by locking their conformation via MOF formation. Such control is unattainable in the solution or crystalline organic materials without constitutional changes.[74]

MOF@FTO films of varying thicknesses were examined by CV. Despite containing both MOF phases, the films' properties seem to be dominated by the DUT-65 phase. This can be derived from the electrochemical behavior (Figure 3) and Raman spectra (Section S8.4). The films with a thickness of ca. 5.2 μm demonstrated superior performance compared to the films with ca. 1, 12, and 28 μm in thickness (Figure S13). While the thinner films exhibited far lower stability and showed a rapid decrease in their redox activity after only 10 cycles (Figure S16), the thicker films exhibited much higher resistances and a stronger diffusion limitation of the observed redox reaction. For this reason, all further characterization was performed with the MOF@FTO films with a thickness of 5 μm. CV scans at different scan speeds allowed for the estimation of the diffusive and capacitive contributions of the observed currents (Figure 4b). The linear relationship of the current to the square root of the scan rate is indicative of a diffusion-controlled process (Figure 4c). Applying the power law (eq S1), slopes of $b = 0.69$ to $b = 0.80$ were determined for the individual oxidation and reduction peaks (Figure 4d).[75,76] These values lie in the transitional region between the ideal diffusive ($b = 0.5$) and ideal capacitive ($b = 1.0$) behaviors.[77,78] The method was also employed separately for the first oxidation step by reversing the potential sweep at 1.2 V vs Ag/Ag$^+$. This allowed the second oxidation step to be excluded from the analysis.

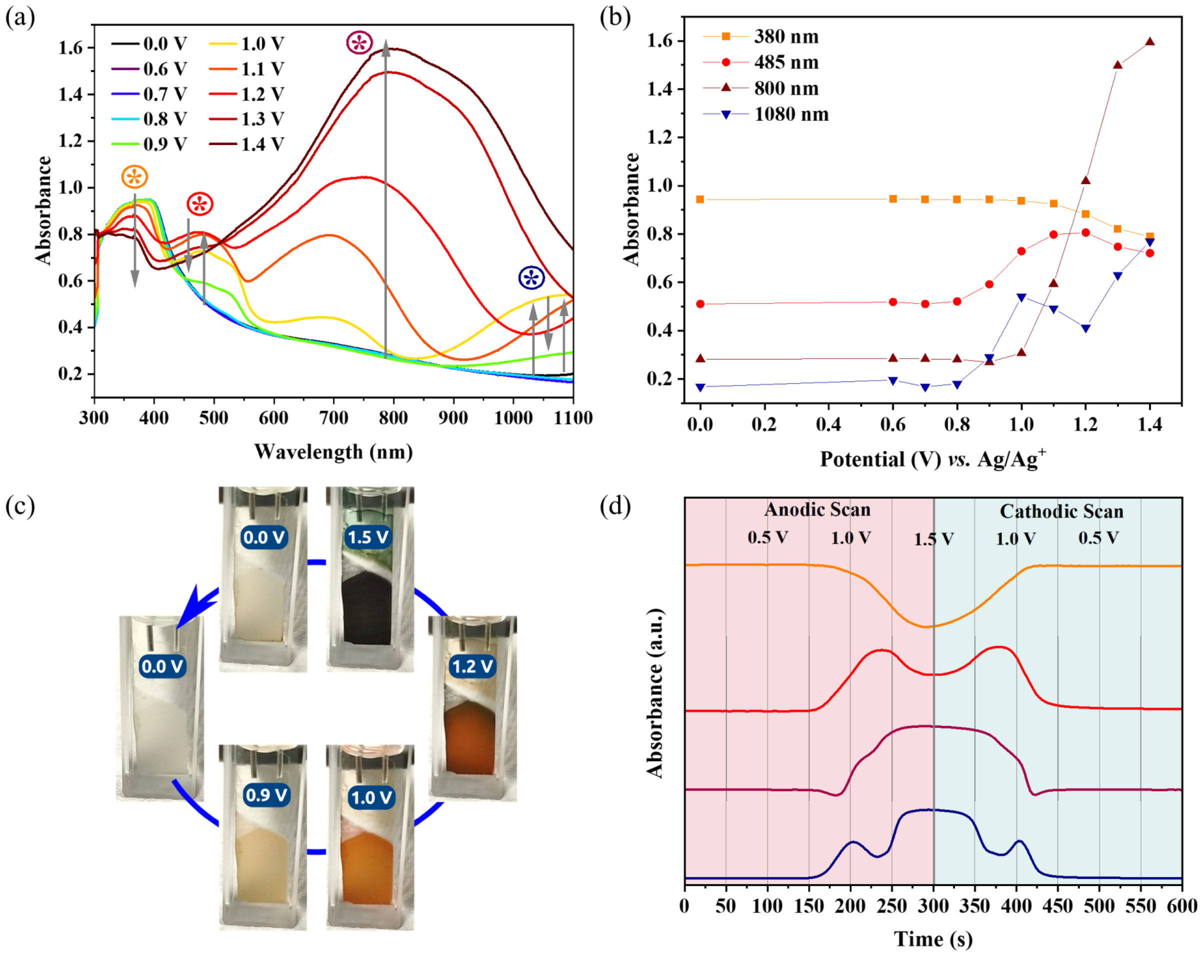

Figure 5. (a) Operando UV−vis spectra obtained at different applied potential. (b) Potential dependent absorbance at the four wavelengths with highest observed absorbance changes (380, 485, 800, and 1080 nm). (c) Photos after 30 s equilibration time at the respective potentials. (d) Kinetic evolution of absorbance at 50 mV/s scan rate. All measured on 5 μm DUT-65/66@FTO films in 0.1 M $TBAPF_6$/ACN vs Ag/Ag^+.

Although a purely diffusion-controlled behavior is expected for a redox-conductive MOF,[12,79−81] very similar *b* values of 0.74 and 0.72 were found for the first oxidation and reduction step, respectively (Figure S13d). However, if the redox reaction occurs predominantly at an interface (e.g., FTO/MOF, or MOF/electrolyte interfaces), the role of the diffusion diminishes.[81] This indicates that not the entire MOF layer participates in the redox process, but only a fractional part.[82]

With the help of Dunn's method (eqs S2 and S3 in Section S7), the two contributions, the diffusive and capacitive, can be distinguished (Figure 4e). The increase in the capacitive contribution with higher scan rates was determined, while the diffusive contribution diminishes accordingly (Figure 4f). At higher scan rates, an even smaller part of the MOF layer engages in the redox reaction. Such behavior is not unexpected for redox-conductive systems. At slow scan rates, enough time is given for the charge carriers to diffuse through the entire MOF layer, thus allowing for the oxidation of all the linkers present. At faster scan rates, the material close to the FTO oxidizes rapidly to the double oxidized state, which is again nonconductive, thus forming an insulating layer and prohibiting continued oxidation of the material further away from the anode.[12,83]

The apparent diffusion coefficient (D_{app}), which is closely correlated to the charge diffusion through the framework, was calculated using the Randles−Sevcik equation (eqs S4−S6, SI section 7)[84] after determining the electroactive surface concentration (Γ_e) through exhaustive oxidation. With Γ_e = 3.18×10^{-8} mol cm^{-2} the diffusion coefficient D_{app} amounts to 2.43×10^{-9} cm^2 s^{-1}. This value is on the higher end of the reported range for other redox-active MOFs, which is unexpected, considering the large size of the PF_6^- anion.[12,13,81,85,86]

To highlight the advantage of an inherently porous material and confirm the stability of the chosen MOF, the CV in an aqueous $LiClO_4$ containing electrolyte of DUT-65/66 on FTO was compared to the $H_4BenzTB$ linker drop-casted on FTO (SI section 7.4). Similar to the organic electrolyte, the MOF demonstrates two distinct oxidation and reduction peaks with very small potential difference ($\Delta E_p < 0.06$ V), indicating rapid diffusion, reversibility of the redox process and stability in aqueous media. In contrast, the linker-based film demonstrates only one oxidation peak and one reduction peak with a very large ΔE_p of over 0.85 V. This clearly indicates the considerable diffusion limitation in the denser amorphous linker film compared to that in the porous MOF.

Spectroelectrochemical Characterization of the DUT-65/66 MOF@FTO Film. The redox activity of the MOF is accompanied by changes in its optical properties. These changes are manifested in the pronounced color change (Figure 5c), shifts in the molecular vibrational frequencies, and changes in fluorescence. These effects were monitored by *operando* UV−vis (Figure 5), Raman spectroscopies, *ex situ* IR-spectroscopy, and *operando* fluorescence spectroscopy (see SI section 8).

In the UV−vis range, the MOF@FTO layer demonstrates the same behavior as that of the linker solution. The MOF film is colorless and transparent in the Vis range in its neutral state and has only a strong absorption band in the UV range of 380 nm. At 0.9 V vs. Ag/Ag$^+$ the alteration in the spectrum starts with a decrease in the intensity of 380 nm band and the appearance of new bands at 485 and >1050 nm. The NIR absorption peak, which is expected at appr. 1390 nm could not be monitored due to technical limitations and manifests itself as the increased absorption at $\lambda > 1050$ nm. The new bands are assigned to the formation of the BenzTB$^{\bullet+}$ species as the colorless film changed to red (Figure 5a,c). With further oxidation (up to 1.5 V vs Ag/Ag$^+$), the absorption at 485 and >1050 nm decreases while an intense broad peak at 800 nm emerges. This indicates the formation of BenzTB^{2+}. The color change is fully reversible, and the MOF film can be bleached again by applying a reducing potential of 0.0 V vs Ag/Ag$^+$. The kinetic evolution of absorbance at the four wavelengths corresponding to the three oxidation states of the linker demonstrates highly symmetrical behavior during oxidation and reduction, which underlines the reversibility of the process (Figure 5d).

Absorption spectra of DUT-65/66@FTO at 800 nm were collected *in situ* by alternately applying 0.0 and 1.5 V vs Ag/Ag$^+$ for 50 s each (Figure 6). The coloration and bleaching response times are determined to be 12.5 and 4.2 s, respectively, to achieve 90% of its full optical modulation (ESI, Figure S17). The 5 μm thick MOF@FTO film exhibits an ultrahigh contrast from the bleaching state (highly transparent neutral form) with transmittance in the visible region >53%, to the colored state with a transmittance of ca. 3%.

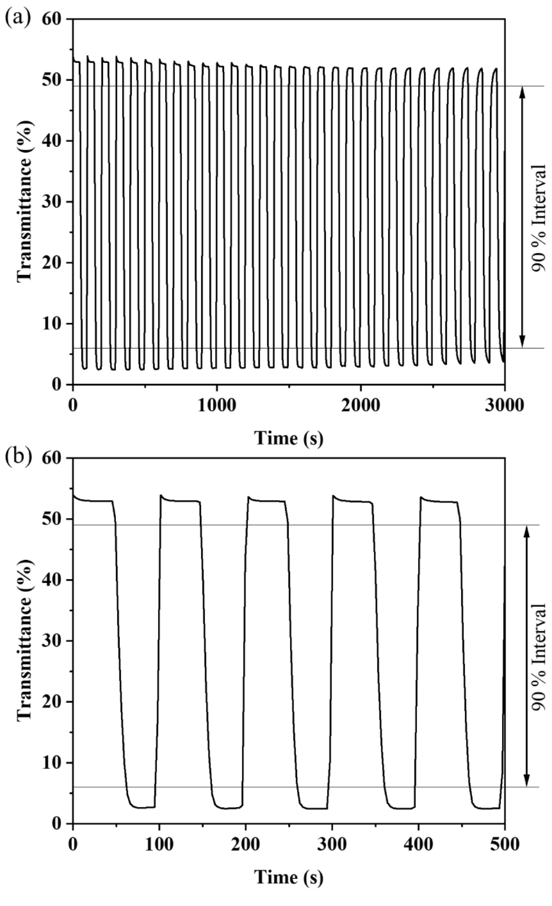

Figure 6. (a) Optical transmittance kinetic curve of the 5 μm DUT-65/66@FTO at 800 nm and (b) zoom of the first 5 cycles.

The reversible coloration and bleaching resulted in only minor degradation within 30 cycles. Utilizing the modified Cottrell equation (eq S8), the kinetics of electron transport through the films could be analyzed (Figure 7). The concentration of oxidized species within the framework can be directly quantified as a function of time by keeping track of the absorbance at 800 nm, which corresponds to the oxidized form of the BenzTB linker.[63,87] The apparent diffusion coefficient (D_{app}) for the system, as determined from the modified Cottrell relation, is only 2.61×10^{-12} cm^2 s^{-1}, which is several orders of magnitude lower than the diffusion coefficient determined from the Randles−Sevcik equation. This discrepancy suggests that the determined electroactive surface concentration (Γ_e) deviates from reality and was likely underestimated (eq S5). This parameter was calculated from the overall charge passed after exhaustive oxidation. However, compared to the geometrically calculated amount of redox active species in the film, it can be determined that only approximately 10% of the film contributes to the redox process during cycling (Section S7.3). Considering this aspect, the reason for deviation of the diffusion coefficient determined with the two above-mentioned methods becomes obvious. The film thickness estimated from the cross-section SEM and used for the Randles−Sevcic equation does not correspond to the film thickness truly engaging in the redox process. As only 10% of the film appear to participate in the redox activity, the d_f value should be asssumed to be 0.52 μm. In this case the Randles−Sevcic equation provides a diffusion coefficient of 2.44×10^{-11} cm^2 s^{-1}, which is much closer to the value obtained from the Cottrell relationship and in line with values for similar MOFs.[12,62,85,86] Considering the polycrystalline nature of the film, the anisotropic diffusion coefficients expected in the given MOF system,[86] and the large size of the PF$_6$$^-$ anion, the value is adequate. Reduction of ions' size can help to further improve the diffusion.[12]

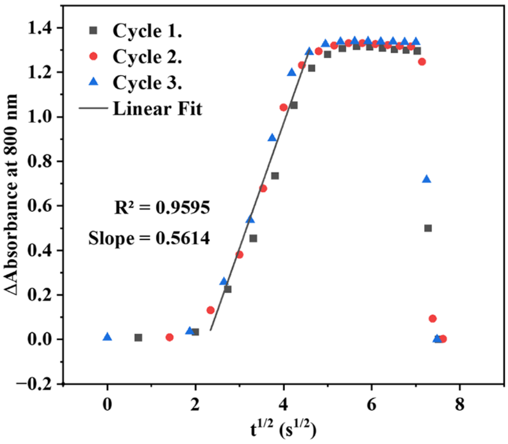

Figure 7. Superimposed Cottrell fits of the first 3 dynamic absorbance response cycles at alternating potential of 0.0 and 1.5 V vs Ag/Ag$^+$ for 50 s each.

Although a thinner film could be potentially beneficial to improve the diffusion, approaching a film thickness of 1 μm causes rapid deterioration during redox cycling. A significant difference in the diffusion coefficient for DUT-65 and DUT-66 is not expected based on the similar limiting pore diameter (9.7 vs 10.2 Å, for DUT-65 and DUT-66 respectively) and earlier published computational studies.[88]

The coloration efficiency (CE) at 800 nm, denoting the ability to generate optical modulations in response to changes in energy or charge, defined as the change in optical density per injected charge density at a particular wavelength, was calculated to be 78 cm^2 C^{-1} (eq S7), which is on par with tungsten oxide based devices.[89−91] Unfortunately, the CE in the NIR range could not be determined.

Upon oxidation, a change in the fluorescence of the films is observed. While the neutral DUT-65/66 films demonstrate a fluorescence with a λ_{max} = 485 nm when excited with a 390 nm wavelength, the fluorescence is completely suppressed upon oxidation. After reduction, the films regain their initial fluorescence (SI section 8.2).

The *in situ* Raman spectroscopy once again confirms the predominantly closed shell state of the oxidized MOF in the film. First, the dicationic form of the MOF exhibits a clear C═N stretching band, while, second, the C−N$^{+\bullet}$ stretching only occurs in the mono-oxidized film (SI section 8.4).

CONCLUSION

Two new chemically stable, porous Zr-based MOFs, involving redox-active tetratopic *N*,*N*,*N′*,*N′*-benzidinetetrabenzoate ligand, were synthesized. The conformational flexibility of the linker leads to the formation of two polymorphs, DUT-65 and DUT-66, containing eclipsed and staggered conformations of the linker, respectively. The polymorphs could be obtained deliberately by adjusting the modulator, synthetic temperature, solvent, or zirconium precursor. Both MOFs demonstrate excellent thermal stability and are stable in aqueous electrolytes. The effect of the different linker conformations on the redox behavior of the MOF was observed for the first time, as manifested in the electronic decoupling of the triarylamine moieties of the linker in the staggered conformation. This unique feature demonstrates a new approach to studying the properties of different conformers without constitutional changes.

The MOF film deposited on the FTO substrate shows excellent electrochromic performance, with a fast electrochromic switching process based on facile access for the electrolyte and ions to the electrochemically active linkers through the MOF pores. The film can be reversibly switched between transparent, red, and virtually black states, while only the red state demonstrates significant absorbance in the NIR range. The film with optimized deposition parameters can realize a transmittance change of 90% and fast switching rate for coloration and bleaching of 12.5 and 4.2 s, respectively. The coloration efficiency of the material is 78 cm^2 C^{-1}. The switching behavior is stable over at least 30 cycles without a noticeable change. Besides the switching of absorption, the fluorescence of the film can be switched on and off via oxidation.

EXPERIMENTAL SECTION

The linker was synthesized according to the published procedure.[53,92] The details can be found in SI section 2.

DUT-65 Single Crystals (S.C. DUT-65). DUT-65 single crystals were obtained by dissolving $ZrCl_4$ (175.3 mg, 752 μmol, 5 equiv) and benzoic acid (8.73 g, 71.5 mmol) in 23 mL of anhydrous DEF through ultrasonication (15 min). To the obtained solution H_4BenzTB (100 mg, 150 μmol, 1 equiv) was added, and the mixture was again sonicated until complete dissolution of the linker (5 min). The clear solution inside a sealed 50 mL Schott flask was placed into a preheated to 120 °C oven for 21 days to yield pale yellow single crystalline material. Yield after cooling to room temperature, washing with DMF (3 × 20 mL), and drying in air for 2 h was 165 mg.

DUT-66 Single Crystals (S.C. DUT-66). These crystals were obtained by dissolving $ZrCl_4$ (175.3 mg, 752 μmol, 5 equiv) and benzoic acid (5.51 g, 45.1 mmol) in 23 mL of anhydrous DMF through ultrasonication (15 min). To the obtained solution H_4BenzTB (100 mg, 150 μmol, 1 equiv) was added, and the mixture was again sonicated until the full dissolution of the linker (5 min). Finally, formic acid (2.25 mL, 60.2 mmol) was added before the clear solution inside a sealed 50 mL Schott flask was placed into a preheated to 80 °C oven for 2 days to yield pale yellow single crystalline material. After washing with DMF (3 × 20 mL) and drying in the air for 2 h, the mass amounted to 150 mg.

DUT-65/66Thin Films on FTO (DUT-65/66@FTO). The films were obtained by first cutting FTO glass into 2.5 × 0.7 cm^2 slides and cleaned by subsequent sonication in Hellmanex, acetone, and Millipore water. The cleaned slides were dried in a nitrogen flow and introduced into a 1 mM solution of H_4BenzTB in DMF (3 mL) overnight at 80 °C in such a way that only half of the FTO slide was immersed in the solution. After cooling down to room temperature, the FTO slides were transferred with their conductive side facing down into scintillation vials (12 mL in volume) with the synthesis solution containing dissolved $ZrCl_4$ (21.0 mg, 90.2 μmol, 2.5 equiv), H_4BenzTB (24.0 mg, 36.1 μmol, 1 equiv), and acetic acid (0.5 mL, 8.7 mmol) in anhydrous DMF (2 mL). The synthesis mixture was then placed in a preheated to 120 °C oven for the respective time between 1 and 72 h (Figure S8). The coated slides were then allowed to cool, washed subsequently with DMF (3 × 5 mL), and left soaking in fresh DMF until further use.

Further experimental details can be found in the Supporting Information.

Crystallographic Data for DUT-65 and DUT-66. The datasets were collected at the BESSY-II synchrotron, operated by Helmholtz−Zentrum Berlin for Materials and Energy.[93]

DUT-65: colorless crystals, $C_{80}H_{48}N_4O_{32}Zr_6$, M_r = 2124.54 g mol^{-1}, orthorhombic, *Cmmm*, a = 19.380(4) Å, b = 29.500(6) Å, c = 20.080(4) Å, V = 11480(4) Å^3, Z = 2, T = 295 K, GooF = 1.192, R_1 ($I > 2\,\sigma(I)$) = 0.0723, wR_2 ($I > 2\sigma(I)$) = 0.2321.

DUT-66: colorless crystals, $C_{80}H_{48}N_4O_{32}Zr_6$, M_r = 2124.54 g mol^{-1}, orthorhombic, *Fmmm*, a = 19.430(4) Å, b = 29.460(6) Å, c = 40.150(8) Å, Z = 4, V = 22982(8) Å, T = 295 K, GooF = 1.068, R_1 ($I > 2\,\sigma(I)$) = 0.0618, and wR_2 ($I > 2\sigma(I)$) = 0.2218.

Accession Codes

CCDC 2339817 (DUT-65) and 2339818 (DUT-66) contain the supplementary crystallographic data for this paper. These data can be obtained free of charge via www.ccdc.cam.ac.uk/data_request/cif., or by emailing data_request@ccdc.cam.ac.uk, or by contacting The Cambridge Crystallographic Data Centre, 12 Union Road, Cambridge CB2 1EZ, U.K.; fax: +44 1223 336 033.

AUTHOR INFORMATION

Corresponding Authors

Irena Senkovska – *Chair of Inorganic Chemistry I, Technische Universität Dresden, 01069 Dresden, Germany;* orcid.org/0000-0001-7052-1029; Email: Irena.Senkovska@tu-dresden.de

Stefan Kaskel – *Chair of Inorganic Chemistry I, Technische Universität Dresden, 01069 Dresden, Germany;* orcid.org/0000-0003-4572-0303; Email: Stefan.Kaskel@tu-dresden.de

Authors

Leonid Shupletsov – *Chair of Inorganic Chemistry I, Technische Universität Dresden, 01069 Dresden, Germany;* orcid.org/0000-0002-2325-9002

Sebahat Topal – *Chair of Inorganic Chemistry I, Technische Universität Dresden, 01069 Dresden, Germany;* Present Address: Institute of Nanotechnology, Karlsruhe Institute of Technology (KIT), Hermann-von-Helmholtz-Platz 1, 76344 Eggenstein-Leopoldshafen, Germany

Alina Schieck – *Chair of Inorganic Chemistry I, Technische Universität Dresden, 01069 Dresden, Germany;* orcid.org/0009-0004-3417-0611

Stella Helten – *Chair of Inorganic Chemistry I, Technische Universität Dresden, 01069 Dresden, Germany*

Ronny Grünker – *Chair of Inorganic Chemistry I, Technische Universität Dresden, 01069 Dresden, Germany;* Present Address: Chair for Molecular Functional Materials, Technische Universität Dresden, Stadtgutstr. 59, 01217 Dresden, Germany

Antareekshya Deka – *Felix Bloch Institute for Solid State Physics, Leipzig University, 04103 Leipzig, Germany*

Ankita De – *Chair of Inorganic Chemistry I, Technische Universität Dresden, 01069 Dresden, Germany;* orcid.org/0000-0003-4962-0510

Matthias Werheid – *Chair of Electrochemistry, Technische Universität Dresden, 01069 Dresden, Germany*

Volodymyr Bon – *Chair of Inorganic Chemistry I, Technische Universität Dresden, 01069 Dresden, Germany;* orcid.org/0000-0002-9851-5031

Inez Weidinger – *Chair of Electrochemistry, Technische Universität Dresden, 01069 Dresden, Germany;* orcid.org/0000-0001-9316-6349

Andreas Pöppl – *Felix Bloch Institute for Solid State Physics, Leipzig University, 04103 Leipzig, Germany;* orcid.org/0000-0003-2354-2542

Author Contributions

#L.S. and S.T. contributed equally.

Funding

DFG (project number 316569666) in the priority program SPP 1928 "COORNETs".

Notes

The authors declare no competing financial interest.

ACKNOWLEDGMENTS

The single crystal X-ray diffraction measurements were carried out at the BL-14.1 and BL-14.2 beamline at the BESSY II electron storage ring operated by the Helmholtz-Zentrum Berlin für Materialien und Energie. We thankfully acknowledge the financial support from HZB.

ABBREVIATIONS

ACN, acetonitrile; BenzTB, *N,N,N′,N′*-benzidinetetrabenzoate; CE, coloration efficiency; COF, covalent organic framework; CV, cyclic voltammogram; D_{app}, apparent diffusion coefficient; DFT, density-functional theory; DCM, dichloromethane; DEF, *N,N*-diethylformamide; DMF, *N,N*-dimethylformamide; DPV, differential pulse voltammetry; DUT, Dresden University of Technology; Fc, ferrocene; FTO, fluorine-doped tin oxide; GC, glassy carbon; HOMO, highest occupied molecular orbital; LUMO, lowest unoccupied molecular orbital; MOF, metal–organic framework; NIR, near-infrared; PVDF, polyvinylidene fluoride; PXRD, powder X-ray diffraction; S.C., single crystal; SEM, scanning electron microscopy; SAM, self-assembled monolayer; SOMO, singly occupied molecular orbital; SET, single electron transfer; $TBAPF_6$, tetrabutylammonium hexafluorophosphate; TD-DFT, time-dependent density functional theory; TCO, transparent conductive oxide; UV–vis, ultraviolet–visible

REFERENCES

(1) Rowsell, J. L.; Yaghi, O. M. Metal–organic frameworks: a new class of porous materials. *Microporous Mesoporous Mater.* **2004**, *73* (1–2), 3–14.

(2) Yaghi, O. M. Reticular Chemistry—Construction, Properties, and Precision Reactions of Frameworks. *J. Am. Chem. Soc.* **2016**, *138* (48), 15507–15509.

(3) Yaghi, O. M. Reticular Chemistry in All Dimensions. *ACS Cent. Sci* **2019**, *5* (8), 1295–1300.

(4) Liu, L.; Xu, Q.; Zhu, Q.-L. Electrically Conductive Metal–Organic Frameworks for Electrocatalytic Applications. *Adv. Energy Sustainability Res.* **2021**, *2* (11), 2100100.

(5) Lin, S.; Usov, P. M.; Morris, A. J. The role of redox hopping in metal-organic framework electrocatalysis. *Chem. Commun.* **2018**, *54* (51), 6965–6974.

(6) Wade, C. R.; Li, M.; Dincă, M. Facile deposition of multicolored electrochromic metal-organic framework thin films. *Angew. Chem., Int. Ed.* **2013**, *52* (50), 13377–13381.

(7) Kung, C. W.; Wang, T. C.; Mondloch, J. E.; Fairen-Jimenez, D.; Gardner, D. M.; Bury, W.; Klingsporn, J. M.; Barnes, J. C.; van Duyne, R.; Stoddart, J. F.; et al. Metal-organic framework thin films composed of free-standing acicular nanorods exhibiting reversible electrochromism. *Chem. Mater.* **2013**, *25* (24), 5012–5017.

(8) Schneider, C.; Ukaj, D.; Koerver, R.; Talin, A. A.; Kieslich, G.; Pujari, S. P.; Zuilhof, H.; Janek, J.; Allendorf, M. D.; Fischer, R. A. High electrical conductivity and high porosity in a Guest@MOF material: evidence of TCNQ ordering within Cu_3BTC_2 micropores. *Chem. Sci.* **2018**, *9* (37), 7405–7412.

(9) Xu, G.; Zhu, C.; Gao, G. Recent Progress of Advanced Conductive Metal-Organic Frameworks: Precise Synthesis, Electrochemical Energy Storage Applications, and Future Challenges. *Small* **2022**, *18* (44), 2203140.

(10) Li, W.-H.; Deng, W.-H.; Wang, G.-E.; Xu, G. Conductive MOFs. *Energy Chem.* **2020**, *2* (2), 100029.

(11) Tao, C.; Li, Y.; Wang, J. The progress of electrochromic materials based on metal–organic frameworks. *Coord. Chem. Rev.* **2023**, *475*, 214891.

(12) Castner, A. T.; Su, H.; Svensson Grape, E.; Inge, A. K.; Johnson, B. A.; Ahlquist, M. S.; Ott, S. Microscopic Insights into Cation-Coupled Electron Hopping Transport in a Metal-Organic Framework. *J. Am. Chem. Soc.* **2022**, *144* (13), 5910–5920.

(13) Li, J.; Kumar, A.; Johnson, B. A.; Ott, S. Experimental manifestation of redox-conductivity in metal-organic frameworks and

its implication for semiconductor/insulator switching. *Nat. Commun.* **2023**, *14* (1), 4388.

(14) Mjejri, I.; Doherty, C. M.; Rubio-Martinez, M.; Drisko, G. L.; Rougier, A. Double-Sided Electrochromic Device Based on Metal-Organic Frameworks. *ACS Appl. Mater. Interfaces* **2017**, *9* (46), 39930−39934.

(15) AlKaabi, K.; Wade, C. R.; Dincă, M. Transparent-to-Dark Electrochromic Behavior in Naphthalene-Diimide-Based Mesoporous MOF-74 Analogs. *Chem* **2016**, *1* (2), 264−272.

(16) Chaudhari, A. K.; Souza, B. E.; Tan, J.-C. Electrochromic thin films of Zn-based MOF-74 nanocrystals facilely grown on flexible conducting substrates at room temperature. *APL Mater.* **2019**, *7* (8), 81101.

(17) Hao, Q.; Li, Z.-J.; Lu, C.; Sun, B.; Zhong, Y.-W.; Wan, L.-J.; Wang, D. Oriented Two-Dimensional Covalent Organic Framework Films for Near-Infrared Electrochromic Application. *J. Am. Chem. Soc.* **2019**, *141* (50), 19831−19838.

(18) Shi, P.; Wang, J.; Guo, Z. A one-dimensional covalent organic framework film for near-infrared electrochromism. *Chem. Eng. J.* **2023**, *451*, 139082.

(19) Liu, J.; Li, M.; Yu, J. High-Performance Electrochromic Covalent Hybrid Framework Membranes via a Facile One-Pot Synthesis. *ACS Appl. Mater. Interfaces* **2022**, *14* (1), 2051−2057.

(20) Bessinger, D.; Muggli, K.; Beetz, M.; Auras, F.; Bein, T. Fast-Switching Vis-IR Electrochromic Covalent Organic Frameworks. *J. Am. Chem. Soc.* **2021**, *143* (19), 7351−7357.

(21) Muggli, K.; Spies, L.; Bessinger, D.; Auras, F.; Bein, T. Electrically Conductive Carbazole and Thienoisoindigo-Based COFs Showing Fast and Stable Electrochromism. *ACS Nanosci. Au* **2023**, *3* (2), 153−160.

(22) Souto, M.; Strutyński, K.; Melle-Franco, M.; Rocha, J. Electroactive Organic Building Blocks for the Chemical Design of Functional Porous Frameworks (MOFs and COFs) in Electronics. *Chem. - Europ. J.* **2020**, *26* (48), 10912−10935.

(23) Ding, B.; Solomon, M. B.; Leong, C. F.; D'Alessandro, D. M. Redox-active ligands: Recent advances towards their incorporation into coordination polymers and metal-organic frameworks. *Coord. Chem. Rev.* **2021**, *439*, 213891.

(24) Radha, G.; Roy, S.; Chakraborty, C.; Aggarwal, H. Electrochromic and photochromic behaviour in a single metal-organic framework containing a redox-active linker. *Chem. Commun.* **2022**, *58* (25), 4024−4027.

(25) Wu, X.; Wang, K.; Lin, J.; Yan, D.; Guo, Z.; Zhan, H. A thin film of naphthalenediimide-based metal-organic framework with electrochromic properties. *J. Colloid Interface Sci.* **2021**, *594*, 73−79.

(26) Lu, Z.; Li, R.; Ping, L.; Bai, Z.; Li, K.; Zhang, Q.; Hou, C.; Li, Y.; Jin, W.; Ling, X.; et al. Ultra-stable ionic-liquid-based electrochromism enabled by metal-organic frameworks. *Cell Rep. Phys. Sci.* **2022**, *3* (5), 100866.

(27) Kumar, A.; Li, J.; Inge, A. K.; Ott, S. Electrochromism in Isoreticular Metal-Organic Framework Thin Films with Record High Coloration Efficiency. *ACS Nano* **2023**, *17* (21), 21595−21603.

(28) Kung, C.-W.; Goswami, S.; Hod, I.; Wang, T. C.; Duan, J.; Farha, O. K.; Hupp, J. T. Charge Transport in Zirconium-Based Metal-Organic Frameworks. *Acc. Chem. Res.* **2020**, *53* (6), 1187−1195.

(29) Liu, J.; Daphne Ma, X. Y.; Wang, Z.; Xu, L.; Xu, T.; He, C.; Wang, F.; Lu, X. Highly Stable and Rapid Switching Electrochromic Thin Films Based on Metal-Organic Frameworks with Redox-Active Triphenylamine Ligands. *ACS Appl. Mater. Interfaces* **2020**, *12* (6), 7442−7450.

(30) Liu, J.; Ma, X. Y. D.; Wang, Z.; Xu, L.; Wang, F.; He, C.; Lu, X. Metal−Organic Framework-Based Flexible Devices with Simultaneous Electrochromic and Electrofluorochromic Functions. *ACS Appl. Electron. Mater.* **2021**, *3* (3), 1489−1495.

(31) Ngue, C. M.; Ho, K. F.; Sainbileg, B.; Batsaikhan, E.; Hayashi, M.; Lee, K. Y.; Chen, R. S.; Leung, M. K. Conductivity and photoconductivity in a two-dimensional zinc bis(triarylamine) coordination polymer. *Chem. Sci.* **2023**, *14* (5), 1320−1328.

(32) Lambert, C.; Nöll, G. The class II/III transition in triarylamine redox systems. *J. Am. Chem. Soc.* **1999**, *121* (37), 8434−8442.

(33) Gomberg, M. AN INSTANCE OF TRIVALENT CARBON: TRIPHENYLMETHYL. *J. Am. Chem. Soc.* **1900**, *22* (11), 757−771.

(34) Tschitschibabin, A. E. Über einige phenylierte Derivate des p, p -Ditolyls. *Ber. Dtsch. Chem. Ges.* **1907**, *40* (2), 1810−1819.

(35) Wieland, H. Über den Mechanismus der blauen Farbreaktion des Diphenylamins. (XVI. Über ditertiäre Hydrazine). *Ber. Dtsch. Chem. Ges.* **1913**, *46* (3), 3296−3303.

(36) Piccard, J. Über Farben zweiter Ordnung und über holo - und meri -chinoide Salze. *Ber. Dtsch. Chem. Ges.* **1913**, *46* (2), 1843−1860.

(37) Piccard, J. Gammes de couleurs et synthèses dans la série du biphényle. *Helv. Chim. Acta* **1924**, *7* (1), 789−799.

(38) Low, P. J.; Paterson, M. A.; Goeta, A. E.; Yufit, D. S.; Howard, J. A.; Cherryman, J. C.; Tackley, D. R.; Brown, B. The molecular structures and electrochemical response of "twisted" tetra(aryl)-benzidenes. *J. Mater. Chem.* **2004**, *14* (16), 2516−2523.

(39) Low, P. J.; Paterson, M. A.; Yufit, D. S.; Howard, J. A.; Cherryman, J. C.; Tackley, D. R.; Brook, R.; Brown, B. Towards an understanding of structure-property relationships in holetransport materials: The influence of molecular conformation on oxidation potential in poly(aryl)amines. *J. Mater. Chem.* **2005**, *15* (23), 2304−2315.

(40) Littleford, R. E.; Tackley, D. R.; Cherryman, J. C.; Dent, G.; Smith, W. E. A Raman and DFT study of substituted triphenylamines for use as charge transfer materials in light emitting polymers. *J. Mol. Struct.* **2004**, *692* (1−3), 81−90.

(41) Low, P. J.; Paterson, M. A. J.; Puschmann, H.; Goeta, A. E.; Howard, J. A. K.; Lambert, C.; Cherryman, J. C.; Tackley, D. R.; Leeming, S.; Brown, B. Crystal, molecular and electronic structure of *N,N′*-diphenyl-*N,N′*-bis(2,4-dimethylphenyl)-(1,1′-biphenyl)-4,4′-diamine and the corresponding radical cation. *Chem.− Eur. J.* **2004**, *10* (1), 83−91.

(42) Kaafarani, B. R.; Risko, C.; El-Assaad, T. H.; El-Ballouli, A. O.; Marder, S. R.; Barlow, S. Mixed-Valence Cations of Di(carbazol-9-yl) Biphenyl, Tetrahydropyrene, and Pyrene Derivatives. *J. Phys. Chem. C* **2016**, *120* (6), 3156−3166.

(43) Ghiglietti, E.; Podapangi, S.; Mecca, S.; Mezzomo, L.; Ruffo, R.; Sassi, M.; Mattiello, S.; Brown, T. M.; Beverina, L. An efficient Buchwald−Hartwig amination protocol enables the synthesis of new branched and polymeric hole transport materials for perovskite solar cells. *Energy Adv.* **2022**, *1* (7), 398−401.

(44) Yuan, W. Z.; Gong, Y.; Chen, S.; Shen, X. Y.; Lam, J. W. Y.; Lu, P.; Lu, Y.; Wang, Z.; Hu, R.; Xie, N.; et al. Efficient Solid Emitters with Aggregation-Induced Emission and Intramolecular Charge Transfer Characteristics: Molecular Design, Synthesis, Photophysical Behaviors, and OLED Application. *Chem. Mater.* **2012**, *24* (8), 1518−1528.

(45) Matis, M.; Rapta, P.; Lukeš, V.; Hartmann, H.; Dunsch, L. Highly charged cations from *N, N,N′,N′*-Tetrakis(4- aminophenyl)-benzidine and Its *N, N,N′,N′*-Tetrakis(4-methoxyphenyl)-Substituted homologue studied by thin-layer in situ electron spin resonance/UV-Vis-NIR spectroelectrochemistry. *J. Phys. Chem. B* **2010**, *114* (13), 4451−4460.

(46) Yang, G.; Zhang, Y.-M.; Cai, Y.; Yang, B.; Gu, C.; Zhang, S. X.-A. Advances in nanomaterials for electrochromic devices. *Chem. Soc. Rev.* **2020**, *49* (23), 8687−8720.

(47) Ni, Y.; Gordillo-Gámez, F.; Peña Alvarez, M.; Nan, Z.; Li, Z.; Wu, S.; Han, Y.; Casado, J.; Wu, J. A Chichibabin's Hydrocarbon-Based Molecular Cage: The Impact of Structural Rigidity on Dynamics, Stability, and Electronic Properties. *J. Am. Chem. Soc.* **2020**, *142* (29), 12730−12742.

(48) Thiele, J.; Balhorn, H. Ueber einen chinoïden Kohlenwasserstoff. *Ber. Dtsch. Chem. Ges.* **1904**, *37* (2), 1463−1470.

(49) Müller, E.; Pfanz, H. Über biradikaloide Terphenylderivate. *Ber. Dtsch. Chem. Ges.* **1941**, *74* (6), 1051−1074.

(50) Ngue, C.-M.; Zhang, Y.-Y.; Leung, M.-K. Exploring redox properties of a 3D Co-based framework with bis(triarylamine)

terphenyl as a redox-active linker. *Chem. Commun.* **2023**, *59* (95), 14157−14160.

(51) Yu, F.; Liu, W.; Ke, S.-W.; Kurmoo, M.; Zuo, J.-L.; Zhang, Q. Electrochromic two-dimensional covalent organic framework with a reversible dark-to-transparent switch. *Nat. Commun.* **2020**, *11* (1), 5534.

(52) Cheon, Y. E.; Park, J.; Suh, M. P. Selective gas adsorption in a magnesium-based metal-organic framework. *Chem. Commun.* **2009**, No. 36, 5436−5438.

(53) Grünker, R.; Senkovska, I.; Biedermann, R.; Klein, N.; Klausch, A.; Baburin, I. A.; Mueller, U.; Kaskel, S. Topological Diversity, Adsorption and Fluorescence Properties of MOFs Based on a Tetracarboxylate Ligand. *Eur. J. Inorg. Chem.* **2010**, *2010* (24), 3835−3841.

(54) Grünker, R.; Senkovska, I.; Biedermann, R.; Klein, N.; Lohe, M. R.; Müller, P.; Kaskel, S. A highly porous flexible Metal-Organic Framework with corundum topology. *Chem. Commun.* **2011**, *47* (1), 490−492.

(55) Felsner, B.; Bon, V.; Evans, J. D.; Schwotzer, F.; Grünker, R.; Senkovska, I.; Kaskel, S. Unraveling the Guest-Induced Switchability in the Metal-Organic Framework DUT-13(Zn). *Chem.- Eur. J.* **2021**, *27* (37), 9708−9715.

(56) Grünker, R.; Bon, V.; Heerwig, A.; Klein, N.; Müller, P.; Stoeck, U.; Baburin, I. A.; Mueller, U.; Senkovska, I.; Kaskel, S. Dye encapsulation inside a new mesoporous metal-organic framework for multifunctional solvatochromic-response function. *Chem.- Eur. J.* **2012**, *18* (42), 13299−13303.

(57) Park, H. J.; Cheon, Y. E.; Suh, M. P. Post-synthetic reversible incorporation of organic linkers into porous metal-organic frameworks through single-crystal-to-single-crystal transformations and modification of gas-sorption properties. *Chem. - Europ. J.* **2010**, *16* (38), 11662−11669.

(58) Li, X.; Jiang, F.; Chen, L.; Wu, M.; Lu, S.; Pang, J.; Zhou, K.; Chen, X.; Hong, M. Two microporous metal−organic frameworks constructed from trinuclear cobalt(II) and cadmium(II) cluster subunits. *CrystEngcomm* **2016**, *18* (13), 2239−2243.

(59) Li, X.; Chen, X.; Jiang, F.; Chen, L.; Lu, S.; Chen, Q.; Wu, M.; Yuan, D.; Hong, M. The dynamic response of a flexible indium based metal-organic framework to gas sorption. *Chem. Commun.* **2016**, *52* (11), 2277−2280.

(60) Song, Q.; Yang, Y.; Yuan, F.; Zhu, S.; Wang, J.; Xiang, S.; Zhang, Z. Electrostatic force-driven lattice water bridging to stabilize a partially charged indium MOF for efficient separation of C_2H_2 /CO_2 mixtures. *J. Mater. Chem. A* **2022**, *10* (17), 9363−9369.

(61) Pang, J.; Yuan, S.; Qin, J.; Liu, C.; Lollar, C.; Wu, M.; Yuan, D.; Zhou, H.-C.; Hong, M. Control the Structure of Zr-Tetracarboxylate Frameworks through Steric Tuning. *J. Am. Chem. Soc.* **2017**, *139* (46), 16939−16945.

(62) Johnson, B. A.; Bhunia, A.; Fei, H.; Cohen, S. M.; Ott, S. Development of a UiO-Type Thin Film Electrocatalysis Platform with Redox-Active Linkers. *J. Am. Chem. Soc.* **2018**, *140* (8), 2985−2994.

(63) Roy, S.; Huang, Z.; Bhunia, A.; Castner, A.; Gupta, A. K.; Zou, X.; Ott, S. Electrocatalytic Hydrogen Evolution from a Cobaloxime-Based Metal-Organic Framework Thin Film. *J. Am. Chem. Soc.* **2019**, *141* (40), 15942−15950.

(64) Connelly, N. G.; Geiger, W. E. Chemical Redox Agents for Organometallic Chemistry. *Chem. Rev.* **1996**, *96* (2), 877−910.

(65) Rapta, P.; Fáber, R.; Dunsch, L.; Neudeck, A.; Nuyken, O. In situ EPR and UV-vis spectroelectrochemistry of hole-transporting organic substrates. *Spectrochim. Acta, Part A* **2000**, *56* (2), 357−362.

(66) Fáber, R.; Mielke, G. F.; Rapta, P.; Staško, A.; Nuyken, O. Anodic oxidation of novel hole-transporting materials derived from tetraarylbenzidines. Electrochemical and spectroscopic characterization. *Collect. Czech. Chem. Commun.* **2000**, *65* (9), 1403−1418.

(67) Su, Y.; Wang, X.; Zheng, X.; Zhang, Z.; Song, Y.; Sui, Y.; Li, Y.; Wang, X. Tuning Ground States of Bis(triarylamine) Dications: From a Closed-Shell Singlet to a Diradicaloid with an Excited Triplet State. *Angew. Chem., Int. Ed.* **2014**, *53*, 2857−2861.

(68) Su, Y.; Wang, X.; Li, Y.; Song, Y.; Sui, Y.; Wang, X. Nitrogen analogues of Thiele's hydrocarbon. *Angew. Chem., Int. Ed.* **2015**, *54* (5), 1634−1637.

(69) O'Keeffe, M.; Yaghi, O. M. Deconstructing the crystal structures of metal-organic frameworks and related materials into their underlying nets. *Chem. Rev.* **2012**, *112* (2), 675−702.

(70) Hausdorf, S.; Baitalow, F.; Seidel, J.; Mertens, F. O. R. L. Gaseous species as reaction tracers in the solvothermal synthesis of the zinc oxide terephthalate MOF-5. *J. Phys. Chem. A* **2007**, *111* (20), 4259−4266.

(71) Bursch, M.; Mewes, J.-M.; Hansen, A.; Grimme, S. Best-Practice DFT Protocols for Basic Molecular Computational Chemistry. *Angew. Chem., Int. Ed.* **2022**, *61*, No. e202205735.

(72) Macrae, C. F.; Sovago, I.; Cottrell, S. J.; Galek, P. T. A.; McCabe, P.; Pidcock, E.; Platings, M.; Shields, G. P.; Stevens, J. S.; Towler, M.; et al. Mercury 4.0: From visualization to analysis, design and prediction. *J. Appl. Crystallogr.* **2020**, *53* (Pt 1), 226−235.

(73) Li, L.; Low, J. Z.; Wilhelm, J.; Liao, G.; Gunasekaran, S.; Prindle, C. R.; Starr, R. L.; Golze, D.; Nuckolls, C.; Steigerwald, M. L.; et al. Highly conducting single-molecule topological insulators based on mono- and di-radical cations. *Nat. Chem.* **2022**, *14* (9), 1061−1067.

(74) Imai, T.; Akasaka, R.; Yoshida, N.; Amaya, T.; Iwasawa, T. Electrochemical and spectroscopic properties of twisted dibenzog,p-chrysene derivatives. *Beilstein J. Org. Chem.* **2022**, *18*, 963−971.

(75) Topal, S.; Savlug Ipek, O.; Sezer, E.; Ozturk, T. Electrochromic-Hybrid energy storage material consisting of triphenylamine and dithienothiophene. *Chem. Eng. J.* **2022**, *434*, 133868.

(76) Wang, K.; Tao, K.; Jiang, R.; Zhang, H.; Liang, L.; Gao, J.; Cao, H. A Self-Bleaching Electrochromic Mirror Based on Metal Organic Frameworks. *Materials* **2021**, *14* (11), 2771.

(77) Naghian, E.; Marzi Khosrowshahi, E.; Sohouli, E.; Ahmadi, F.; Rahimi-Nasrabadi, M.; Safarifard, V. A new electrochemical sensor for the detection of fentanyl lethal drug by a screen-printed carbon electrode modified with the open-ended channels of Zn(II)-MOF. *New J. Chem.* **2020**, *44* (22), 9271−9277.

(78) Liu, J.; Wang, J.; Xu, C.; Jiang, H.; Li, C.; Zhang, L.; Lin, J.; Shen, Z. X. Advanced Energy Storage Devices: Basic Principles, Analytical Methods, and Rational Materials Design. *Adv. Sci.* **2018**, *5* (1), 1700322.

(79) Shimoni, R.; He, W.; Liberman, I.; Hod, I. Tuning of Redox Conductivity and Electrocatalytic Activity in Metal−Organic Framework Films Via Control of Defect Site Density. *J. Phys. Chem. C* **2019**, *123* (9), 5531−5539.

(80) Hod, I.; Sampson, M. D.; Deria, P.; Kubiak, C. P.; Farha, O. K.; Hupp, J. T. Fe-Porphyrin-Based Metal−Organic Framework Films as High-Surface Concentration, Heterogeneous Catalysts for Electrochemical Reduction of CO_2. *ACS Catal.* **2015**, *5* (11), 6302−6309.

(81) Lin, S.; Pineda-Galvan, Y.; Maza, W. A.; Epley, C. C.; Zhu, J.; Kessinger, M. C.; Pushkar, Y.; Morris, A. J. Electrochemical Water Oxidation by a Catalyst-Modified Metal-Organic Framework Thin Film. *ChemSuschem* **2017**, *10* (3), 514−522.

(82) Shen, C.-H.; Chuang, C.-H.; Gu, Y.-J.; Ho, W. H.; Song, Y.-D.; Chen, Y.-C.; Wang, Y.-C.; Kung, C.-W. Cerium-Based Metal-Organic Framework Nanocrystals Interconnected by Carbon Nanotubes for Boosting Electrochemical Capacitor Performance. *ACS Appl. Mater. Interfaces* **2021**, *13* (14), 16418−16426.

(83) Johnson, B. A.; Beiler, A. M.; McCarthy, B. D.; Ott, S. Transport Phenomena: Challenges and Opportunities for Molecular Catalysis in Metal-Organic Frameworks. *J. Am. Chem. Soc.* **2020**, *142* (28), 11941−11956.

(84) Sezer, E.; Turksoy, F.; Tunca, U.; Ozturk, T. Electrochemical behaviour of some BEDT-TTF and TTF derivatives. *J. Electroanal. Chem.* **2004**, *570* (1), 101−105.

(85) Duan, J.; Goswami, S.; Hupp, J. T. Redox-Hopping-Based Charge Transport Mediated by Ru(II)-Polypyridyl Species Immobilized in a Mesoporous Metal-Organic Framework. *Front. Chem. Eng.* **2022**, *3*, 828266.

(86) Goswami, S.; Hod, I.; Duan, J. D.; Kung, C.-W.; Rimoldi, M.; Malliakas, C. D.; Palmer, R. H.; Farha, O. K.; Hupp, J. T. Anisotropic Redox Conductivity within a Metal-Organic Framework Material. *J. Am. Chem. Soc.* **2019**, *141* (44), 17696−17702.

(87) Ahrenholtz, S. R.; Epley, C. C.; Morris, A. J. Solvothermal preparation of an electrocatalytic metalloporphyrin MOF thin film and its redox hopping charge-transfer mechanism. *J. Am. Chem. Soc.* **2014**, *136* (6), 2464−2472.

(88) Bukowski, B. C.; Snurr, R. Q. Topology-Dependent Alkane Diffusion in Zirconium Metal-Organic Frameworks. *ACS Appl. Mater. Interfaces* **2020**, *12* (50), 56049−56059.

(89) Wang, S.; Xu, H.; Hao, T.; Xu, M.; Xue, J.; Zhao, J.; Li, Y. 3D conifer-like WO3 branched nanowire arrays electrode for boosting electrochromic-supercapacitor performance. *Appl. Surf. Sci.* **2022**, *577*, 151889.

(90) Wang, Z.; Wang, X.; Cong, S.; Chen, J.; Sun, H.; Chen, Z.; Song, G.; Geng, F.; Chen, Q.; Zhao, Z. Towards full-colour tunability of inorganic electrochromic devices using ultracompact fabry-perot nanocavities. *Nat. Commun.* **2020**, *11* (1), 302.

(91) Lee, S.; Kim, M. J.; Lee, S. H.; Jeong, S. H.; Kwon, J. H.; Jeong, J. K. Boosting coloration efficiency in an electrochromic device using an ITO/Ag/ITO multilayered electrode and porous WO 3 chromic layer. *J. Inf. Dispersion* **2023**, *24* (3), 177−188.

(92) Wolfe, J. P.; Buchwald, S. L. Palladium-catalyzed amination of aryl halides and aryl triflates: *N*-hexyl-2-methyl-4-methoxyaniline and *N*-methyl-*N*-(4-chlorophenyl)aniline. *Org. Synth.* **2002**, *78*, 23.

(93) Mueller, U.; Darowski, N.; Fuchs, M. R.; Förster, R.; Hellmig, M.; Paithankar, K. S.; Pühringer, S.; Steffien, M.; Zocher, G.; Weiss, M. S. Facilities for macromolecular crystallography at the Helmholtz-Zentrum Berlin. *J. Synchrotron Radiat.* **2012**, *19* (Pt 3), 442−449.